2024 IEEE/RSJ International Conference on Intelligent Robots and Systems (IROS)
October 14-18, 2024. Abu Dhabi, UAE

IMU Based Pose Reconstruction and Closed-loop Control for Soft Robotic Arms

Guanran Pei[1,3], Francesco Stella [1,2], Omar Meebed[1],
Zhenshan Bing[3], Cosimo Della Santina[2,4], Josie Hughes[1]

***Abstract*— Soft continuum manipulators are celebrated for their versatility and physical robustness to external forces and perturbations. However, this feature comes at a cost. The many degrees of freedom and compliance pose challenges for accurate pose reconstruction, both in terms of distributed sensing and pose reconstruction algorithms. Moreover, soft arms are inherently susceptible to deformation from external forces or loads, meaning that closed-loop control is essential for robust task performance. In this article, we propose the integration of multiple Inertial Measurement Units (IMUs) of a soft robot arm, Helix, for reconstruction of pose under internal and external forces. Furthermore, we integrate this dynamic pose reconstruction for kinematic-based closed-loop control strategies. By serially integrating sensing in the body of the Helix soft manipulator, we provide the system with high-frequency pose reconstruction and demonstrate improvements in end effector position with comparison to open-loop performance.**

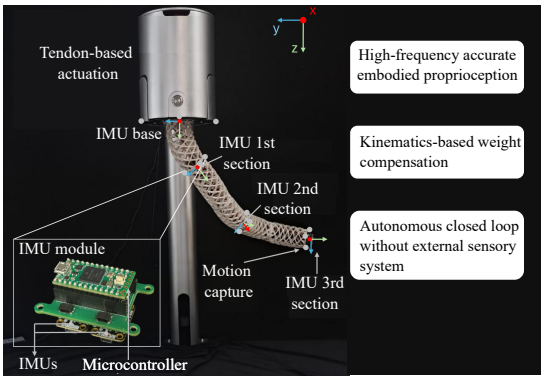

Fig. 1. The embedded IMU shape reconstruction system enables high-frequency, precise proprioception and closed-loop kinematic control for the Helix soft manipulator.

I. Introduction

Soft robotic arms offer significant advantages over rigid ones, including greater compliance, flexibility, and a larger workspace [1], [2]. They also pose a lower risk and enable smoother interactions with humans [3], [4]. However, to maximize these benefits and achieve effective task completion, their precision and resilience to external disturbances must be enhanced. This necessitates pose reconstruction methods that accurately capture the full 3D configuration of the soft robot arm, allowing for precise closed-loop control in both static and dynamic tasks [5].

The compliance and flexibility of soft robotic arms create challenges for designing effective proprioceptive systems. One solution is to use external sensors for pose reconstruction and closed-loop control, such as computer vision and external motion capture systems [6]–[8]. While these sensors can provide high-precision dynamic motion reconstruction, they require calibration and are limited by outdoor conditions and occlusions. Alternatively, embedded sensors can be used, including cable measurements for shape deformation [9], Fiber Bragg Grating (FBG) sensor nodes for strain computation [10], and customized soft sensors for deformation detection [11]–[13]. Consequently, much research on soft manipulators relies on open-loop controllers or closed-loop controllers using motion capture methods [5].

[1]CREATE Lab, EPFL, Lausanne, Switzerland. [2]Department of Cognitive Robotics, Delft University of Technology, Delft, The Netherlands. [3]Technical University of Munich, Munich, Germany. [4]Institute of Robotics and Mechatronics, German Aerospace Center (DLR), Wessling, Germany. This project was partially supported by the EU's research and innovation program EMERGE. Contact email: josie.hughes@epfl.ch.

The Inertial Measurement Unit (IMU) is increasingly integrated into soft robots for pose reconstruction, demonstrated in both single-section [14], [15] and complex soft manipulators [16]. Building on this approach, we propose combining IMU-based sensing with encoder position information for accurate pose reconstruction of a large-scale soft manipulator [17]. IMUs provide high-frequency sampling to capture dynamic motions and reconstruct the robot's full 3D configuration. Coupled with a model-based closed-loop controller, this enables static and dynamic closed-loop control, as shown in Figure 1. In summary, the main contributions of this paper are:

1) Development of an embedded IMU module, which enables real-time pose reconstruction and closed-loop control of the soft manipulator.
2) Characterization of the IMU and encoder-based soft robot reconstruction, and the model-based controller performance.
3) Demonstration of the feasibility of achieving precise pose control for large-scale soft manipulators without external sensors, thereby expanding their application scenarios.

In the remainder of this article, we first introduce the PCC model, the pose reconstruction algorithm, and the closed-loop design. In Section III we detail the design and integration of the IMUs into the soft robot arm. Finally, in Section IV we provide the experimental results followed by a Discussion and Conclusion.

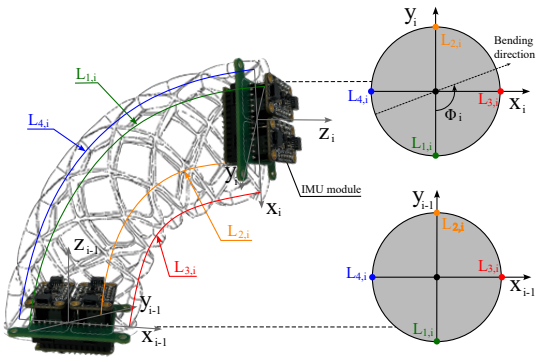

Fig. 2. Piecewise constant curvature Model with improved parametrization [18]. $L_{1,i}$ and $L_{2,i}$, which are located on the surface of the soft section and intersect with X_{i-1} and X_i and parallel to the central line, are used to represent the bending of the soft section in the y-axis direction through their difference $\Delta_{\mathrm{y},i}$. Similarly, $L_{3,i}$ and $L_{4,i}$ are used to compute the difference $\Delta_{\mathrm{x},i}$ representing the bending of the soft section in the x-axis direction.

II. Methods

In this study, we focus on using a model-based approach for shape reconstruction and closed-loop control of soft manipulators.

A. Piecewise Constant Curvature Model

The soft manipulator was modeled using a piecewise constant curvature (PCC) model [19], with improved parametrization by Della Santina *et al.* [18]. Each actuation section was parametrized as shown in Figure 2. For controller development, three spaces were defined: tendon L, configuration S, and Cartesian X. Each section is fully defined by tendon lengths $L = [l_1, l_2, l_3]$, configuration Lagrangian variables $S = [s, \Delta_\mathrm{x}, \Delta_\mathrm{y}]$ for bending deformation, and Cartesian variables $X = [x, y, z]$ for the end effector's position. The forward kinematics FK_{l2s} from L to S space is defined to move between these spaces.

$$\begin{aligned}
\kappa &= 2\frac{\sqrt{l_1^2+l_2^2+l_3^2-l_1l_2-l_2l_3-l_1l_3}}{d\left(l_1+l_2+l_3\right)} & \Delta_\mathrm{x} &= \kappa s\cos\phi \\
\phi &= \tan^{-1}\left(\frac{\sqrt{3}}{3}\frac{l_3+l_2-2l_1}{l_2-l_3}\right) & \Delta_\mathrm{y} &= \kappa s\sin\phi \\
s &= \frac{l_3+l_2+l_1}{3}
\end{aligned} \tag{1}$$

where κ and ϕ denote the soft section's curvature and bending orientation, respectively; d represents the distance between the tendons and the central line of the soft section; and Δ_x and Δ_y describe the bending of the soft section in the x and y directions. Additionally, the forward kinematics FK_{s2x} from S to X for the i-th section can be formulated according to [18], with the tip position being mappable through

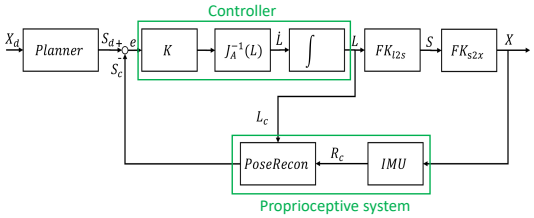

Fig. 3. Kinematic closed-loop control block diagram consists of IK-planner, proprioceptive system and controller.

$$t_{i-1}^{i}\left(\Delta_{\mathrm{x},i},\Delta_{\mathrm{y},i},L_i,s_i\right) = \frac{L_i}{\Delta_i^2}\begin{bmatrix}\left(1-\cos\left(s_i\Delta_i\right)\right)\Delta_{\mathrm{x},i}\\ \left(1-\cos\left(s_i\Delta_i\right)\right)\Delta_{\mathrm{y},i}\\ \sin\left(s_i\Delta_i\right)\Delta_i\end{bmatrix} \tag{2}$$

in which $\Delta_i = \sqrt{\Delta_{\mathrm{x},i}^2+\Delta_{\mathrm{y},i}^2}$.

B. IMU based Pose Reconstruction Algorithm

The PCC model allows the bending parameters $\Delta_{\mathrm{x},i}$ and $\Delta_{\mathrm{y},i}$ to be reconstructed from IMUs using the algorithm proposed in [14]. This study introduces a method for reconstructing the pose of a soft section by solving an optimization problem.

$$\arg\min_{\Delta_{\mathrm{x},i},\Delta_{\mathrm{y},i}\in\mathbb{R}^2}\left\|R_{i-1}^{i}\left(\Delta_{\mathrm{x},i},\Delta_{\mathrm{y},i}\right)-\hat{R}_{i-1}^{i}\right\|_\mathrm{F}^2 \tag{3}$$

in which $\|\cdot\|_F$ is the Frobenius norm, and $R_{i-1}^{i}\left(\Delta_{\mathrm{x},i},\Delta_{\mathrm{y},i}\right)$ is PCC model-based tip orientation, and $\hat{R}_{i-1}^{i}$ is the real orientation between the tip and base. As shown in Figure 2, the IMU modules measure the relative orientation between the base and tip. The initial guess of the optimization problem is

$$\begin{aligned}
\Delta_{\mathrm{x},i} &= \frac{\frac{1}{2}\left(\hat{R}_{i-1}^{i}[3,1]-\hat{R}_{i-1}^{i}[1,3]\right)\arccos\left(\hat{R}_{i-1}^{i}[3,3]\right)}{\sin\left(\arccos\left(\hat{R}_{i-1}^{i}[3,3]\right)\right)}\\
\Delta_{\mathrm{y},i} &= \frac{\frac{1}{2}\left(\hat{R}_{i-1}^{i}[3,2]-\hat{R}_{i-1}^{i}[2,3]\right)\arccos\left(\hat{R}_{i-1}^{i}[3,3]\right)}{\sin\left(\arccos\left(\hat{R}_{i-1}^{i}[3,3]\right)\right)}
\end{aligned} \tag{4}$$

In this optimization problem, we fit the PCC model to the actual tip orientation by optimizing the parameters of the rotation matrix $R_{i-1}^{i}\left(\Delta_{\mathrm{x},i},\Delta_{\mathrm{y},i}\right)$. This allows us to derive the shape parameters $\Delta_{\mathrm{x},i}$ and $\Delta_{\mathrm{y},i}$ of the soft section based on the PCC model.

C. Closed-loop Control Design

Leveraging the IMU-based reconstruction algorithm and the encoders of the actuation motors, the configuration variables s, Δ_x and Δ_y of soft manipulators can be fully reconstructed. To ensure reliable end effector's position control, we designed a kinematic control loop using inverse kinematics to generate target tendon lengths, with the IMU-based reconstruction closing the loop.

As shown in Figure 3, the closed-loop control of the end effector in Cartesian space involves three components: an inverse kinematics (IK) planner that maps Cartesian to configuration space, IMU-based reconstruction, and a closed-loop controller based on the PCC model using the current

robot pose. For a soft manipulator modeled with the PCC model, the forward kinematics from tendon space through configuration space to the end effector in Cartesian space is given by the following equation.

$$X = FK_{s2x}(S) = FK_{s2x}\left(FK_{l2s}\left(L\right)\right) \tag{5}$$

Thus, $\mathbf{J}_A$, the Jacobian matrix from L to S can be represented as:

$$\dot{S} = \frac{\partial FK_{l2s}}{\partial L}\dot{L}(t) = \mathbf{J}_A(L)\dot{L} \tag{6}$$

where $\dot{S}$, $\dot{L}$ represent the first-order derivatives of variables in configuration and tendon space, respectively. Furthermore, To control the soft manipulator to the target configuration, S_d can be transformed to solve the optimization problem as shown in equation (7) by using the first-order resolved rate algorithm iteratively [20].

$$L_d = \underset{L}{\operatorname{argmin}} \left\| S_d - FK_{l2s}(L) \right\| \tag{7}$$

where L_d is the target tendon length for the desired configuration S_d. The formula for iteratively updating the controller to approximate S_d from the current configuration S_j is as follows.

$$L_{j+1} = L_j + J_A^{-1}\left(L_i\right) K \left(S_d - S_j\right) \tag{8}$$

where L_j and S_j represent the tendon length and configuration at the j-th iteration, respectively, and K is the proportional constant. The IK-planner converts the Cartesian end-effector pose to the corresponding configurations. The model-based controller then updates the tendon lengths to achieve the target configuration by evaluating the error between the target and current configurations which are reconstructed by the IMU-based algorithm.

III. EXPERIMENTAL METHODS

A. IMU Module Design

To facilitate modular integration into soft robot arms, we have developed a compact IMU unit. As shown in Figure 1, the IMU module includes two 9-degree-of-freedom (DoF) IMU sensors (LSM6DSDX + LIS3MDL, Adafruit), a miniature Teensy 4.0 microcontroller (MCU), and a small connecting PCB. Through I2C bus The MCU processes raw data from the IMU's gyroscope, accelerometer, and magnetometer using the Madgwick filter for orientation correction [21], which mitigates drift from gyroscope angular velocity integration and sensor errors.

B. IMU Integration

The IMU modules were mounted at the end of each segment to provide orientation data for reconstruction, as shown in Figure 1. By reconstructing the shape of each soft section, the overall shape of the soft manipulator can be reconstructed. All four IMU modules were connected to a single I2C bus, managed by a master microcontroller that accessed and collected orientation data from each IMU. This data, along with the nine tendon lengths, was sent to a central computer to solve pose reconstruction and compute motor control signals as detailed in Section II-B and II-C. The hardware achieves an average IMU sensing frequency of 55.8 Hz and average shape reconstruction and control frequencies of 27.4 Hz and 26.6 Hz, respectively, over 1000 iterations.

Before the experiment begins, the entire system is calibrated in the following way: All tendons of the soft arm are tightened through current control of the actuation motors. Based on the orientation data from the IMUs, each section is manually adjusted to be slightly compressed and free of bending deformation. The motor positions in this state, along with the trunk length of each section measured using motion capture, are recorded as reference values for subsequent experiments.

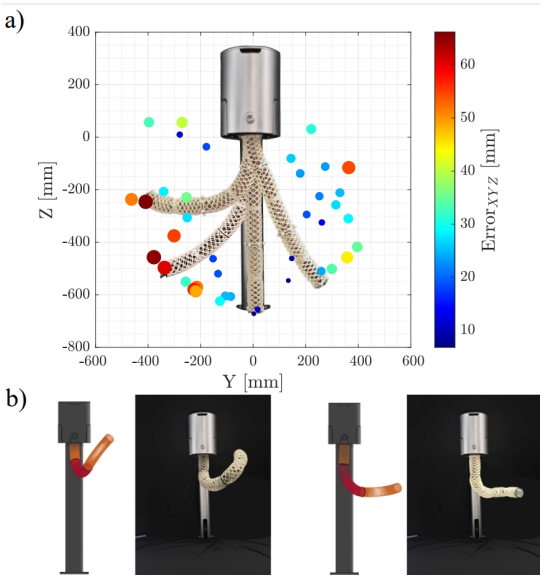

Fig. 4. a) Distribution graph of errors between the real end effector positions recorded by motion capture and IMU-based reconstructions for 40 poses spread across the soft manipulator workspace. b) IMU-based 3D shape reconstruction and real manipulator configurations.

IV. EXPERIMENTAL RESULTS

A. IMU-based Reconstruction

To characterize the IMU-based reconstruction, we benchmark its performance in the static and dynamic scenarios.

1) Static Pose Reconstruction Accuracy: To benchmark performance variation across the robot's workspace, we initially tested IMU-based reconstruction in static configurations. We selected 40 uniformly distributed end effector positions in the Y-Z plane and sequentially drove the soft manipulator to each position. After stabilization, we reconstructed the pose using IMU data and obtained the ground truth from a motion capture system, calculating the reconstruction error across the workspace.

As shown in Figure 4, the average 3D IMU reconstruction error is 31.5 mm, or 4.5% of the soft manipulator's full length. The average 2D IMU reconstruction error in the Y-Z plane is 19.4 mm, or 2.8% of the full length. Generally, IMU-based reconstruction shows larger errors for sampling

points at the outer edges of the workspace. This is primarily due to bending in the first section, leading to propagation errors caused by IMU drift of the first section.

To validate the 3D reconstruction of the entire robot, not just the end effector, we compared visualizations of the reconstructed robot to the real poses for various poses. These poses were carefully selected to represent extreme cases of 3D bending, which are the most challenging for reconstruction. Figure 4 shows both the reconstructed and real-world photos of the manipulator. Even with significant 3D bending, the reconstruction accurately captures the deformations in each section, as well as the end effector.

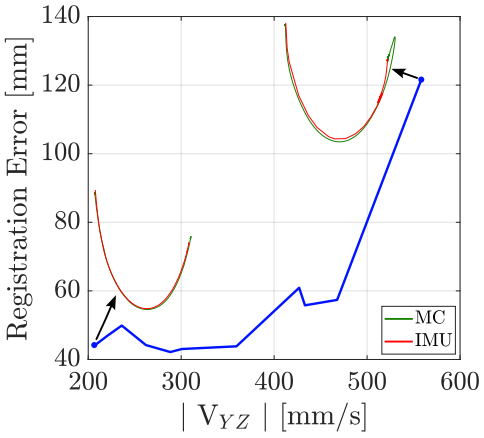

Fig. 5. The line graph depicting the variation of 1D registration error between motion capture and IMU trajectories with the absolute change in end effector velocity. The curves in the bottom left and top right corners respectively represent the trajectories recorded by motion capture and IMUs for the end effector at the highest and lowest speeds.

2) Dynamic IMU-Based Reconstruction: Beyond the static pose reconstruction test, we demonstrate the IMU-based proprioceptive system's ability to reconstruct poses in various dynamic scenarios. This capability is crucial for tasks like human-robot interaction and object manipulation, highlighting the advantage of using IMUs. To assess the impact of dynamics on reconstruction, we compared results at different motion speeds. We set a start and end target pose for the end effector in the Y-Z plane of the base coordinate system, interpolated a specified number of points between them, and used open-loop inverse kinematics to reach these poses. By varying the number of points, the robot's speed ranged from 207 to 558 mm/s.

By reconstructing the soft manipulator's trajectory using both IMUs and motion capture, we can determine the error in IMU-based reconstruction as arm motion speed increases. Figure 5 illustrates the trajectories at the slowest and fastest speeds, showing that greater discrepancies occur with more dynamic motion. To quantify and compare the IMU reconstruction, we applied 1D registration to align the motion capture trajectory with the IMU trajectory. The point-to-point distance between these aligned trajectories serves as the registration error, as shown in Figure 5. While registration error increases with speed, it remains low until reaching 500 mm/s.

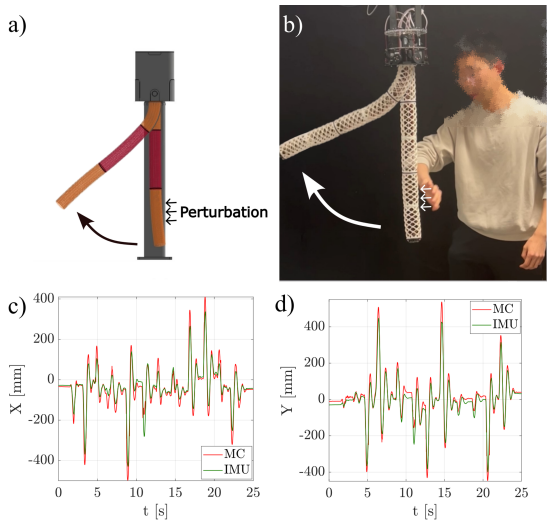

Fig. 6. a): Dynamic deformations of the soft manipulator caused by external perturbation through IMU-based reconstruction. b): Real dynamic deformations of the soft manipulator caused by external perturbation. c), d): The trajectory of the end effector in the x-y plane over time recorded by motion capture and reconstructed by the IMU-based proprioceptive system.

3) Reconstructing External Disturbances: The IMU-based reconstruction can not only sense dynamic trajectories but also detect configuration changes due to external 3D perturbations. To assess this response, the soft arm's tendons are relaxed and operated in current control mode, with real-time posture sensed via IMUs and motor encoders. External perturbations are applied by a human, as shown in Fig. 6 a) and b). Fig. 6 c) and d) depict the time series response of the end effector's X and Y positions for both IMU and motion capture data. Although tracking the exact amplitude of each minimum and maximum is challenging, the IMUs' measurement frequency effectively captures high-frequency disturbances.

B. IMU-enabled Closed-Loop Control

In this subsection, we characterize the closed-loop controller under static and dynamic conditions and compare the closed-loop performance to the open-loop performance.

1) Static Closed-Loop Control: We first evaluate static pose performance using closed-loop control to benchmark it against open-loop performance. Twenty target end effector positions within the soft manipulator's workspace were selected. The manipulator was moved to these target poses sequentially using both controllers, with the robot's position recorded via a motion capture system. The position control error was determined by computing the distance between the actual and desired end effector positions in the Y-Z plane. As shown in Figure 7 a) and b), the closed-loop controller had an average 3D control error of 33 mm (4.8% of the full length), with maximum and minimum errors of 50 mm and 9.6 mm, respectively. In contrast, the open-loop controller exhibited an average error of 163 mm (23.3% of the full length), with maximum and minimum errors of 273 mm

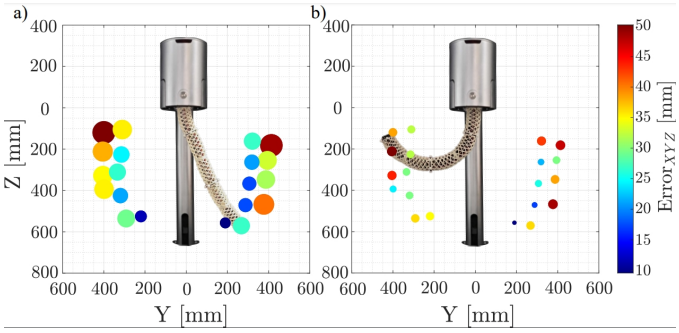

Fig. 7. a): Distribution graph of end effector pose and Cartesian error achieved through open-loop controller for static soft manipulator pose control. b): Distribution graph of end effector pose and Cartesian error achieved through closed-loop controller for static soft manipulator pose control.

and 62 mm, respectively. The open-loop controller's average error was approximately five times greater than that of the closed-loop controller. However, both controllers demonstrated lower precision in the upper workspace area. This is due to the increasing influence of the soft manipulator's self-weight, making it difficult for the kinematics control. For the closed loop control, IMU drift causes directional errors when reconstructing the bending deformation of the soft sections.

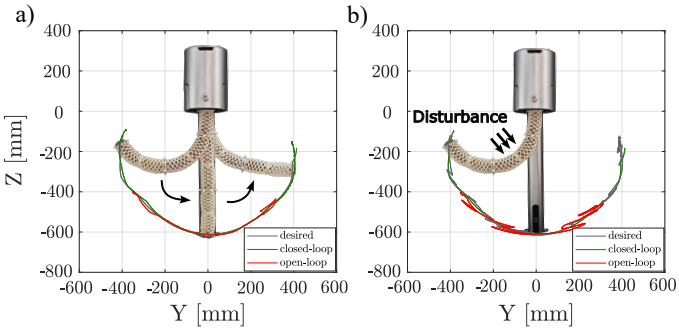

Fig. 8. a) Comparison of real end effector trajectories following the desired trajectory using open- and closed-loop controllers. b) The response of open- and closed-loop controllers to random external disturbances (externally applied instantaneous force disturbances at any location, direction, and magnitude on the soft arm) during trajectory following.

2) Dynamic Closed-loop Control: To demonstrate control precision in dynamic scenarios, we created a trajectory by linearly interpolating between 10 static poses within the robot's workspace. The soft manipulator was then controlled to follow this target trajectory using both open-loop and closed-loop controllers, with the motion capture system recording the end effector's position. By comparing the actual trajectories with the desired one, we assessed the trajectory tracking performance of both controllers. As shown in Figure 8 a), both controllers track the desired trajectory well at the bottom of the soft manipulator's workspace. However, precision decreases for both controllers as trajectories move toward the middle and upper regions. The open-loop controller struggles to reach the upper parts of the desired trajectory due to the influence of self-weight, while the closed-loop controller successfully reaches the end

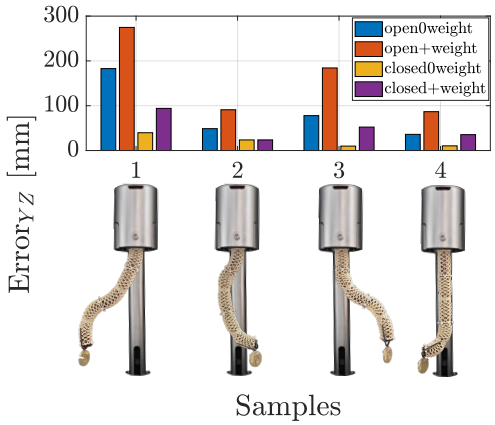

Fig. 9. Comparison of the static pose control accuracy of the soft manipulator using open-loop and closed-loop controllers with and without payload at the end effector.

target configuration regardless of the robot's self-weight.

We also evaluated the trajectory tracking performance of the soft manipulator under random external disturbances using both open- and closed-loop controllers, to simulate more dynamic and real-world conditions. Using the same trajectory as in the previous experiment, random external force disturbances were applied to each section of the manipulator. The comparison of the desired and measured trajectories shows the resistance of the closed-loop controller to disturbances. As illustrated in Figure 8 b), the closed-loop control maintained clear tracking of the desired trajectory despite random external disturbances, demonstrating resilience and inherent stability. In contrast, the open-loop control, which depends solely on the passivity of the soft manipulator, resulted in trajectories that deviated significantly from the desired path, appearing chaotic and disordered.

3) Weight compensation: In addition to compensating for self-weight, the closed-loop controller can also handle external loads, which is crucial for practical applications like pick-and-place tasks. We benchmarked the "payload compensation" feature for both static and dynamic scenarios. For static scenarios, we added a 300g mass to the end effector in four representative poses and measured the error between the target and actual positions for both open- and closed-loop controllers, with and without the weight. Figure 9 shows that the closed-loop controller demonstrates significantly higher control precision compared to the open-loop controller, regardless of the payload. For more bent poses (sample 1 and 3), the closed-loop controller's precision is approximately three times higher than the open-loop controller's, both with and without payload. For positions at the bottom of the workspace (sample 2 and 4), the precision of the closed-loop controller remains significantly better, although the gap narrows. For dynamic scenarios, we used sample 1 and sample 3 from the static pose experiment to generate a smooth trajectory for the end effector. The soft manipulator followed this trajectory using both open- and closed-loop controllers, with and without weight. A motion capture

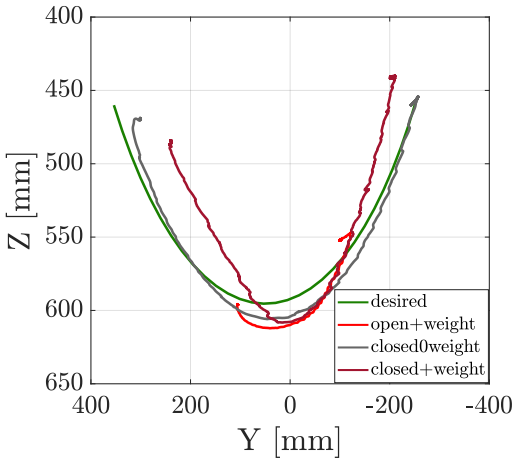

Fig. 10. Real end effector trajectories recorded by motion capture during trajectory following using open-loop and closed-loop controllers with and without payload at the end effector.

system recorded configurations of the soft arm and the end effector's positions.

As shown in Figure 10, the open-loop control performs poorly in tracking the desired trajectory when the end effector carries the weight. In contrast, the closed-loop controller effectively controls the soft manipulator for precise trajectory following, regardless of the load. The trajectory with the payload is compressed in the Y-axis direction and stretched towards the direction of gravity. This occurs due to two reasons: the payload causes additional deformation in the direction of gravity, shortening the soft manipulator on the deformed side. Additionally, the control of the soft manipulator's posture is based on a three-degree-of-freedom PCC model, while the manipulator has infinite degrees of deformation freedom. This limitation prevents tracking all deformations, such as shear forces induced by gravity, which do not alter the trunk length or the tip's orientation relative to the base. Controllers based on the PCC model cannot effectively track and compensate for such deformations.

V. Discussion and Conclusion

This study proposed and tested an IMU-based proprioceptive system and closed-loop controller for a continuum soft robot. The pose reconstruction algorithm achieved an accuracy of 4.5% of the robot's length for static positions and provided precise, high-frequency tracking of dynamic motions. The study compared open- and closed-loop control strategies to evaluate the control precision in static and dynamic scenarios. The closed-loop control strategy demonstrated superior pose control precision and better resistance and compensation to external disturbances compared to the open-loop controllers. In conclusion, the IMU-based reconstruction offered a precise, high-frequency, and embedded sensing and control possibility of soft manipulators. Future work will focus on extending current pose reconstruction strategies to higher-order models, such as polynomial curvature models [22]. Further research will explore how precise pose reconstruction using embedded IMUs can serve as a foundation for human-robot interaction studies.

References

[1] D. Rus and M. T. Tolley, "Design, fabrication and control of soft robots," *Nature*, vol. 521, no. 7553, pp. 467–475, 2015.

[2] H. Jiang, Z. Wang, Y. Jin, X. Chen, P. Li, Y. Gan, S. Lin, and X. Chen, "Design, control, and applications of a soft robotic arm," *arXiv preprint arXiv:2007.04047*, 2020.

[3] F. Stella and J. Hughes, "The science of soft robot design: A review of motivations, methods and enabling technologies," *Frontiers in Robotics and AI*, vol. 9, p. 1059026, 2023.

[4] C. Lee, M. Kim, Y. J. Kim, N. Hong, S. Ryu, H. J. Kim, and S. Kim, "Soft robot review," *International Journal of Control, Automation and Systems*, vol. 15, pp. 3–15, 2017.

[5] J. Wang and A. Chortos, "Control strategies for soft robot systems," *Advanced Intelligent Systems*, vol. 4, no. 5, p. 2100165, 2022.

[6] R. M. Monteiro, J. Shi, H. Wurdemann, F. Iida, and T. G. Thuruthel, "Visuo-dynamic self-modelling of soft robotic systems," 2023.

[7] E. Almanzor, F. Ye, J. Shi, T. G. Thuruthel, H. A. Wurdemann, and F. Iida, "Static shape control of soft continuum robots using deep visual inverse kinematic models," *IEEE Transactions on Robotics*, 2023.

[8] L. Scimeca, J. Hughes, P. Maiolino, and F. Iida, "Model-free soft-structure reconstruction for proprioception using tactile arrays," *IEEE Robotics and Automation Letters*, vol. 4, no. 3, pp. 2479–2484, 2019.

[9] M. D. Grissom, V. Chitrakaran, D. Dienno, M. Csencits, M. Pritts, B. Jones, W. McMahan, D. Dawson, C. Rahn, and I. Walker, "Design and experimental testing of the octarm soft robot manipulator," in *Unmanned Systems Technology VIII*, vol. 6230. International Society for Optics and Photonics, 2006, p. 62301F.

[10] Z. Zhang, X. Wang, S. Wang, D. Meng, and B. Liang, "Shape detection and reconstruction of soft robotic arm based on fiber bragg grating sensor array," in *2018 IEEE International Conference on Robotics and Biomimetics (ROBIO)*. IEEE, 2018, pp. 978–983.

[11] T. Kim, S. Lee, T. Hong, G. Shin, T. Kim, and Y.-L. Park, "Heterogeneous sensing in a multifunctional soft sensor for human-robot interfaces," *Science robotics*, vol. 5, no. 49, p. eabc6878, 2020.

[12] I. Van Meerbeek, C. De Sa, and R. Shepherd, "Soft optoelectronic sensory foams with proprioception," *Science Robotics*, vol. 3, no. 24, p. eaau2489, 2018.

[13] S. Y. Kim, Y. Choo, R. A. Bilodeau, M. C. Yuen, G. Kaufman, D. S. Shah, C. O. Osuji, and R. Kramer-Bottiglio, "Sustainable manufacturing of sensors onto soft systems using self-coagulating conductive pickering emulsions," *Science robotics*, vol. 5, no. 39, p. eaay3604, 2020.

[14] J. Hughes, F. Stella, C. D. Santina, and D. Rus, "Sensing soft robot shape using imus: An experimental investigation," in *Experimental Robotics: The 17th International Symposium*. Springer, 2021, pp. 543–552.

[15] Y. Meng, G. Fang, J. Yang, Y. Guo, and C. C. Wang, "Spring-imu fusion-based proprioception for feedback control of soft manipulators," *IEEE/ASME Transactions on Mechatronics*, 2023.

[16] R. Peng, Y. Wang, and P. Lu, "A tendon-driven continuum manipulator with robust shape estimation by multiple imus," *IEEE Robotics and Automation Letters*, 2024.

[17] Q. Guan, F. Stella, C. Della Santina, J. Leng, and J. Hughes, "Trimmed helicoids: an architectured soft structure yielding soft robots with high precision, large workspace, and compliant interactions," *npj Robotics*, vol. 1, no. 1, p. 4, 2023.

[18] C. Della Santina, A. Bicchi, and D. Rus, "On an improved state parametrization for soft robots with piecewise constant curvature and its use in model based control," *IEEE Robotics and Automation Letters*, vol. 5, no. 2, pp. 1001–1008, 2020.

[19] B. A. Jones and I. D. Walker, "Kinematics for multisection continuum robots," *IEEE Transactions on Robotics*, vol. 22, no. 1, pp. 43–55, 2006.

[20] B. Siciliano, L. Sciavicco, L. Villani, and G. Oriolo, *Force control*. Springer, 2009.

[21] S. Madgwick *et al.*, "An efficient orientation filter for inertial and inertial/magnetic sensor arrays," *Report x-io and University of Bristol (UK)*, vol. 25, pp. 113–118, 2010.

[22] C. Della Santina and D. Rus, "Control oriented modeling of soft robots: the polynomial curvature case," *IEEE Robotics and Automation Letters*, vol. 5, no. 2, pp. 290–298, 2019.